Stony Brook University

Carbon dioxide multiphase flow in microfluidic devices

A Thesis Presented

by

Ruopeng Sun

to

The Graduate School
in partial fulfillment of the Requirements
for the Degree of

Master of Science
In
Mechanical Engineering

Stony Brook University
December 2010

Stony Brook University
The Graduate School

Ruopeng Sun

We, the thesis committee for the above candidate for the Master of Science degree,
Hereby recommend acceptance of this thesis.

Dr. Thomas Cubaud, Thesis Advisor,
Assistant Professor, Mechanical Engineering Department

Dr. Jon Longtin, Chairperson of defense,
Associate Professor, Mechanical Engineering Department

Dr. John Kincaid, Committee Member,
Professor, Mechanical Engineering Department

This thesis is accepted by the Graduate School

Lawrence Martin

Dean of the Graduate School

Abstract of the Thesis

Carbon dioxide multiphase flow in microfluidic devices

by

Ruopeng Sun

Master of Science

in

Mechanical Engineering

Stony Brook University

2010

In this thesis, we experimentally studied the mass transfer during CO_2 absorption into water, ethanol, methanol and silicone oil under slug flow in microchannels. We showed that the initial bubble size is determined by the liquid fraction and channel geometry, while the CO_2 diffusion rate is determined by the gas pressure and liquid properties, such as the Henry's constant and the diffusion coefficient. The reduction of the gas void fraction α_G along the flow direction and the transformation of segmented flows into dilute bubbly flows was observed and predicted. In high viscosity liquids, we showed the liquid film thickness is related to the capillary number and the gas pressure. We also constructed experimental setup for investigating CO_2 cavitation in microchannels. A linear time dependence of bubble growth from depressurization is observed. In addition, we proposed the fabrication procedure of co-flowing capillary tip and listed its current limitations.

Table of Contents

List of Figures

List of Tables

ACKNOWLEDGEMENTS

It is a pleasure for me to thank those who made this thesis possible. First I would like to thank Prof. Thomas Cubaud, for his guidance and invaluable support throughout my academic and research term at Stony Brook University. Also I want to thank Prof. Jon Longtin and Prof. John Kincaid for agreeing to be part of my thesis committee member. Last but not the least, I want to thank my colleague at Microfluidic Lab, Samira and Bibin for the kindness help.

As a graduate student at Stony Brook University, I have learned a lot and grown as a mature person in the past two and half years. Stony Brook University provides me an inspiring environment to explore the unknowns. I am now confident and well rounded in all specialties and have a vision of how I see myself grow in the future.

Chapter 1

1. Introduction

Microfluidic devices enable the manipulation of fluids and pattern surfaces at small length scales [1]. It provides advantages in many applications, ranging from the life sciences industries (drug discovery, delivery and detection, and diagnostic devices) to the chemical engineering industries (rapid chemical analyses and high throughput screening). The use of smaller sample volume significantly reduces the cost and waste [2].Typically, microfluidics refers to devices or flow configurations that have the smallest design feature on the scale of the order of micron. For liquid composed of small molecules, such as water, this scale is still suited with the continuum assumption, although the surface forces play a more important role than in macroscale.

Multiphase flow in microfluidic devices has been the subject of increased research interest in the past decades [3-5 6 7]. Due to its advantage of the large interfacial area, multiphase microchemical system is encountered in many important applications, such as enhanced mixing and multiphase reactors [8, 9].

In gas-liquid multiphase flows, one of the most common two-phase flow pattern in microchannels is the slug flow, which consists of elongated bubbles with equivalent diameters usually several times of the channel width, separated by liquid plugs[5]. The bubbles adopt a characteristic capsular shape. They almost completely fill the channel cross section, and are only

separated from the wall by a thin liquid film[6]. The large unit volume gas-liquid interfacial area of slug bubble gives its unique advantage of enhancing interfacial mass transfer. In addition, because the bulk liquid is separated by the gas bubbles, axial mixing between the separated liquid slugs is significantly reduced. The mass transfer from gas to liquid, however, is improved by the recirculation of the liquid slug between bubbles. [10]

1.1. Review of forces and gas diffusion process

1.1.1 Laminar condition

Most of the microfluidic experiments yield to the scale of 1μm~1mm, which allows the use of the continuous medium assumption, such as the Navier-Stokes equation:

$$\rho \frac{DU}{Dt} = -\nabla P + \eta \nabla^2 U \tag{1-1}$$

where ρ is the fluid density, η is the dynamic viscosity, P is the pressure, and U is the velocity.

Eq(1-1) can be nondimensionalized as:

$$\frac{D'U'}{Dt'} = -\nabla' P' + \frac{1}{Re} \nabla'^2 U' \tag{1-2}$$

which gives a dimensionless factor, Reynolds number, defined by the ratio of inertia forces over viscous forces.

$$Re = \frac{UL}{\nu} \tag{1-3}$$

where ν is the kinematic viscosity defined as the dynamic viscosity η over the density ρ, L is the characteristic length, and U is the mean fluid velocity.

Typically in microfluidic devices, the length scale is about 1μm~1mm, the flow speed, which varies widely from different experiments, is in the range of cm/s, which yields *Re* ~*O*(1). Such a small Reynolds number indicates that viscous forces dominate inertia forces, and the flow regime is laminar, rather than turbulent.

In turbulent flow, mixing is enhanced by the development of the instabilities. However, in laminar flow, instabilities are damped out by the viscous force, the characteristic time for mixing is governed by the diffusion alone.

1.1.2 Capillary force.

Another important force in multiphase flows in microchannels is the interfacial force. The Capillary number *Ca*, defined as the ratio between the viscous force and the surface tension, is the most important dimensionless number in droplet formation

$$Ca = \frac{\eta U}{\gamma} \tag{1-4}$$

where γ is the surface tension between two fluids. In typical microfluidic devices, the *Ca* is also small due to the small length scale and low fluid velocity ($Ca < O(10)$).

1.1.3 Fick's law of binary diffusion

Diffusion is a key factor which governs the mixing process in microfluidic devices. The molecular transport of one substance into another is called mass diffusion. Adolf Fick derived a law which relates the diffusive flux to the concentration gradient:

$$\mathbf{J} = -\rho D \nabla C \tag{1-5}$$

where D is the molecular diffusivity or coefficient of diffusion and **J** is the diffusion flux. D is proportional to the squared velocity of the diffusing particles, which depends on the temperature, viscosity of the fluid and the size of the particles.

1.1.4 Henry's law

For the gas diffusion in liquids, another key parameter besides the diffusivity is the solubility of gases in solvents. For liquid-gas systems, the gas diffusion dynamic is not only governed by the diffusion law but also limited by the solubility. Henry's law states that the solubility of a gas phase at constant temperature is proportional to the gas partial pressure, which can be mathematically formed as:

$$P_G = Hg\, C \tag{1-6}$$

where P_G is the gas pressure and Hg is the Henry's constant. The Henry's constant depends on the solute, the solvent and the temperature.

1.2 Geometry of microfluidic bubble formation section

Several simple geometries have been implemented for producing bubbles and droplets in microfluidic devices [Fig. 1.1]. These include the focusing mechanism, the cross-flowing rupture technique and the co-flowing geometry. Since these device mix liquid and gas continuously, they can be categorized as the passive mixers that do not require any moving parts.

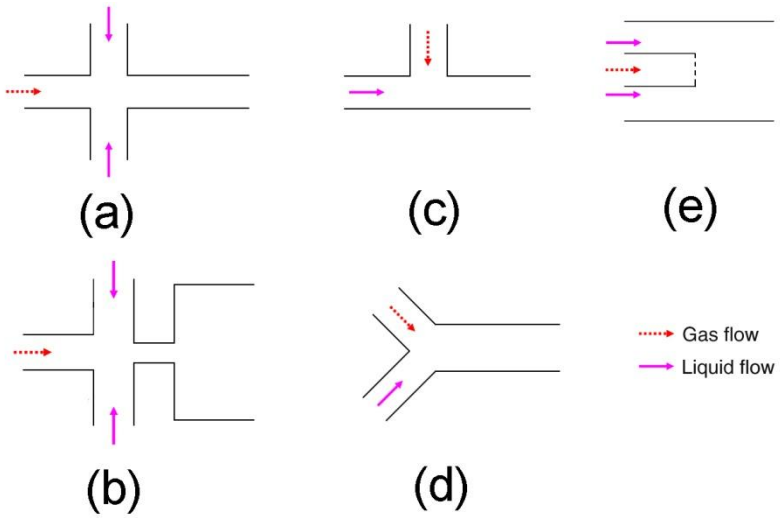

Fig. 1.1 Schematic of typical microfluidic junctions. (a) Hydrodynamic focusing. (b) Flow-focusing. (c) T-junction. (d) Y-junction. (e) Co-flowing.

1.2.1 Cross-flowing

The cross-flowing geometry often refers to the T-junctions and Y-junctions[Fig. 1.1 (c)(d)]. The mixing section contains one continuous phase inlet and one dispersed phase inlet. This breakup mechanism has been proved to have good uniformity in the size of the produced bubbles. The key control parameters for bubbles or droplets generation are the ratio of liquid/gas flow rate and the capillary number *Ca*. Thorsen *et al* [11] used T-junctions to generate water droplets in oil. They found when the dispersed phase pressure P_d is comparable to the continuous phase pressure P_c, the droplet size is proportional to P_d, while when pressure difference between two phase are significant, no droplets was formed.

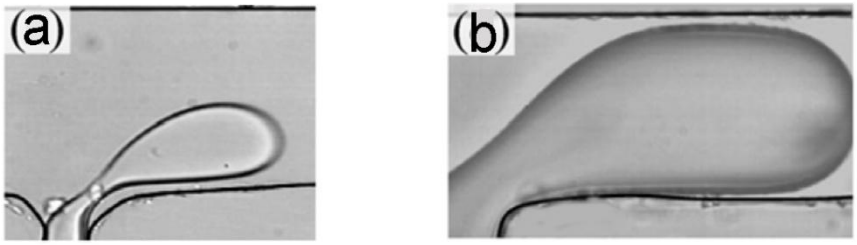

Fig. 1.2 Image of droplet breakup in T-junction. (a) Unconfined breakup.(b) Confined breakup. [12]

The bubble formation in the T-junction can be further categorized as unconfined breakup and confined breakup. The confined breakup refers to the case in which the formed thread of dispersed phase blocks the entire continuous phase, and thus its development is confined by the channel geometry. As the dispersed obstruction forms, the upstream liquid pressure is increased. The liquid pressure increase would eventually collapse and pinch-off the gas thread to form a bubble. Gastecki *et al* [13] reported that the size of bubbles or droplets is related to the dispersed/continuous flow rate ratio. This breakup mechanism is also called as squeezing [14]. Unconfined breakup refers to the case in which dispersed phase thread does not fill out the entire channel's cross section, and the bubbles breakup are mainly controlled by the local shear stress. Normally, this phenomenon appears when the dispersed phase inlet's width is much smaller than the continuous phase inlet [15]. This regime is also called as dripping regime [14]. Some researchers [15] [13] [16] found that the bubbles size depends on the capillary number, in addition to the gas/liquid flow ratio and the viscosity contrast.

1.2.2 Focusing Geometry

The focusing configuration can be classified into two types: (I) with an orifice, (II) without an orifice. Both type mixers have three inlets and one outlet, the central inlet is for the dispersed phase, and two symmetrical side inlets are filled with the continuous phase liquid. The main difference is geometry I has a narrow neck between inlets and outlet, while geometry II has uniform sized inlets and outlet. Generally, geometry I is called the flow focusing geometry, geometry II is called the hydrodynamic focusing[17 18]

The formation of bubbles or droplets in flow-focusing geometry is related to the capillary instability. Ganan-Calvo [19] studied geometry I at the macroscale, and correlated bubble diameter to the liquid/gas flow rate ratio with a power index 0.37. Anna *et al* [20] implemented the flow focusing mixing into the microscale. Jensen *et al* [21] investigated numerically of the bubble break up and correlated the gas pressure, liquid flow rate, channel size, surface tension and liquid viscosity to the bubble size. Garstecki *et al* [22] proposed the bubble collapse rate at neck is quasi stationary and related to the liquid flow rate. They also correlated the volume of bubbles with the liquid flow rate, gas pressure and liquid viscosity. Dollet *et al* [23] also studied bubble break up at this geometry and reached a conclusion that inertial force, rather than the capillary force, is the key reason for bubble breakup.

Cubaud *et al* [18] adapted the hydrodynamic focusing geometry using four straight square microchannels and proposed a scaling law of the bubble length based on the mean bubble velocity times the liquid pinch off time. The pinch time can be calculated as the channel width divided by the superficial liquid velocity. They show that the bubble size is inversely proportional to the liquid fraction. Dietrich *et al* [24] compared the bubble formation at cross shape side channel geometry and the converged side channels geometry.

1.2.3 Co-flowing

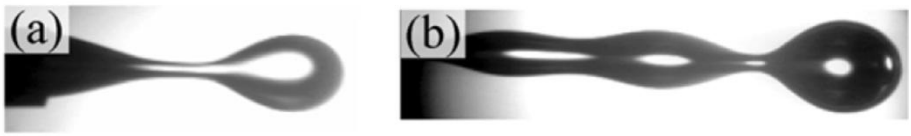

Fig. 1.3 Image of droplet breakup in co-flowing streams. (a) Dripping.(b) Jetting. [25]

The co-flowing geometry (also named centerline injection) introduces the dispersed phase from the center channel or capillary, and the dispersed flowing stream is paralleled to the continuous flowing stream. Cramer *et al* [25] conducted droplet break up experiment by inserting a micro capillary into a minichannel. Similar to other geometries, they found two breakup mechanisms: (1) dripping, (2) jetting. Dripping refers to the phenomenon that droplet breakup right at the capillary tip, while in jetting regime, a long thread was formed downstream before the droplet breakup. Marin *et al* [26] found that steady conical tip formed when bubbles break up from the center tip and no gas jetting forms in a wide range of capillary number (~10). They also observed that the bubble size can be as small as 1/10 of the injection needle.

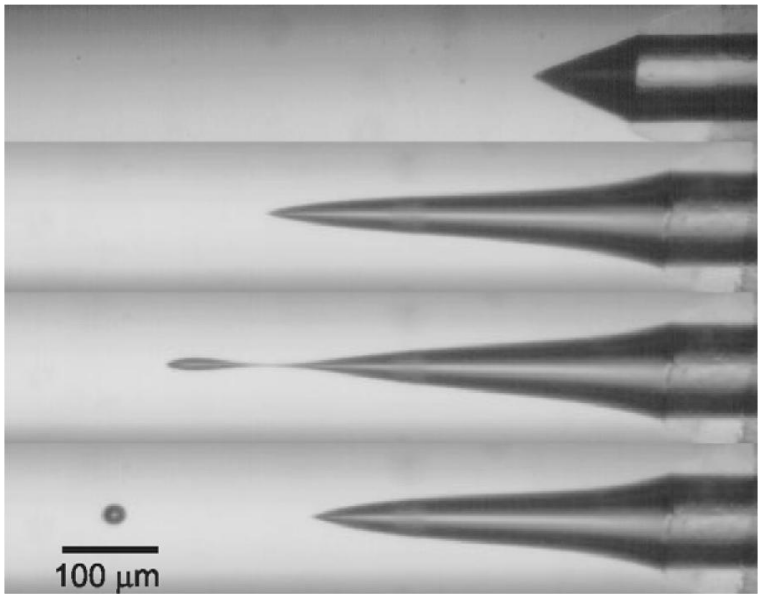

Fig. 1.4 Image of micron sized bubble generation from Co-flowing geometry. [26]

1.3 Flow patterns

Depending on the method for generating bubbles, different flow maps have been proposed. [27, 28] Based on the relative importance of the liquid and gas superficial velocity, the flow regimes of two phase flow in microchannels can be identified as: surface tension dominated, inertia dominated and transitional regime. These three flow regimes consist of many flow patterns, and different researchers gave different names to these patterns. For example, Slug flow [29], Taylor flow [6] and bubble train flow [30] basically refer to the same pattern. Regardless of the lack of uniformity in the terminology, there are three major flow patterns in microchannels: bubbly flow, slug flow and annular flow. There are also two other flow patterns, churn flow and dispersed flow, which are inertia-dominated and are not very common at the microscale.

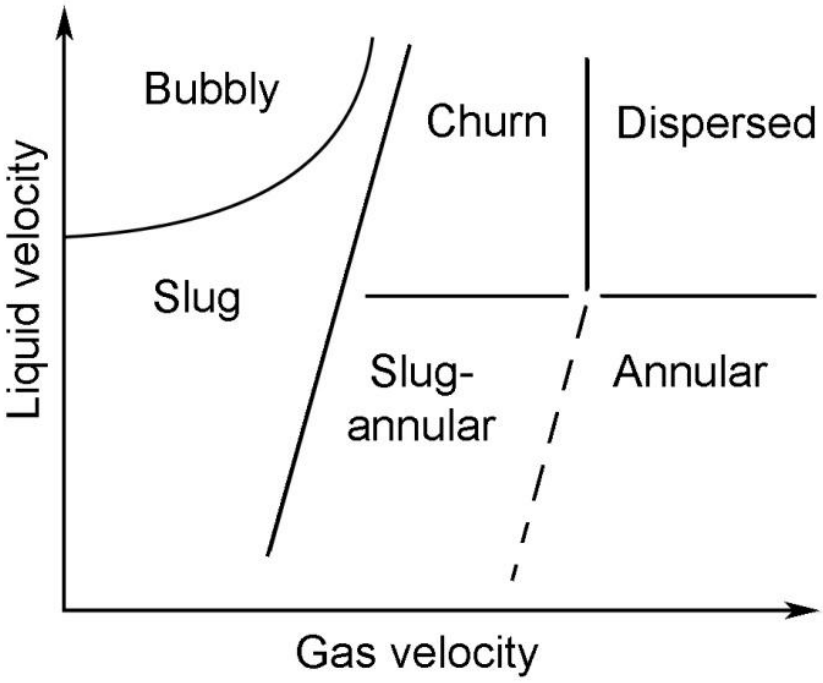

Fig. 1.5 Typical flow pattern in microchannels.

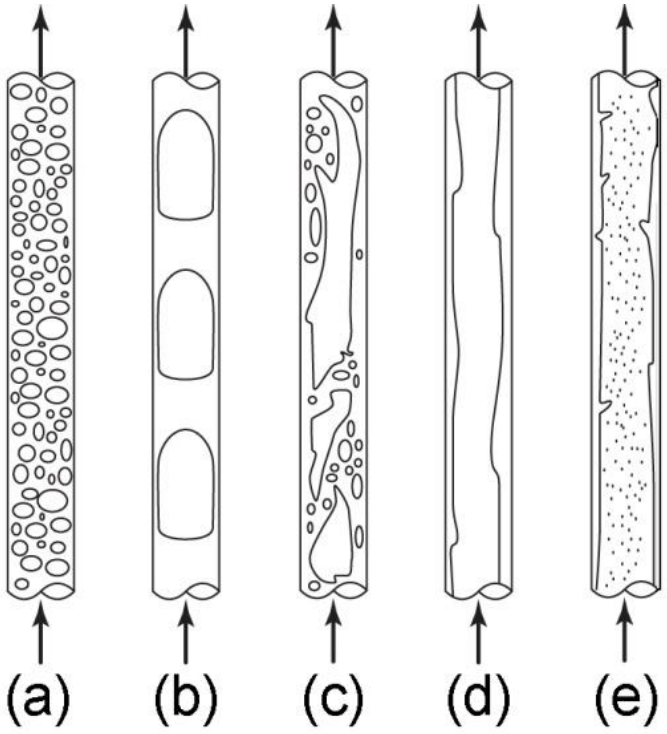

Fig. 1.6 Sketch of observed flow patterns in microchannels [31]. (a) Bubbly flow,(b) Slug flow, (c) Churn flow, (d) Annular flow, (e) Dispersed flow

1.3.1 Bubbly flow:

In bubbly flow, the non wetting gas flow forms small bubbles (normally considerably smaller than the channel or capillary diameter), which are dispersed in the continuous wetting liquid. As individual bubbles may collide and coalesce with each other to form larger bubbles, polydispersity was observed [27]. This pattern exists at high liquid superficial velocities and low gas superficial velocities, as shown in Fig.1.5. Cubaud and Ho [27] found that for low liquid velocity, bubble clogging occurs in sharp corner bends which can easily trap a small bubble, as shown in Fig.1.7.

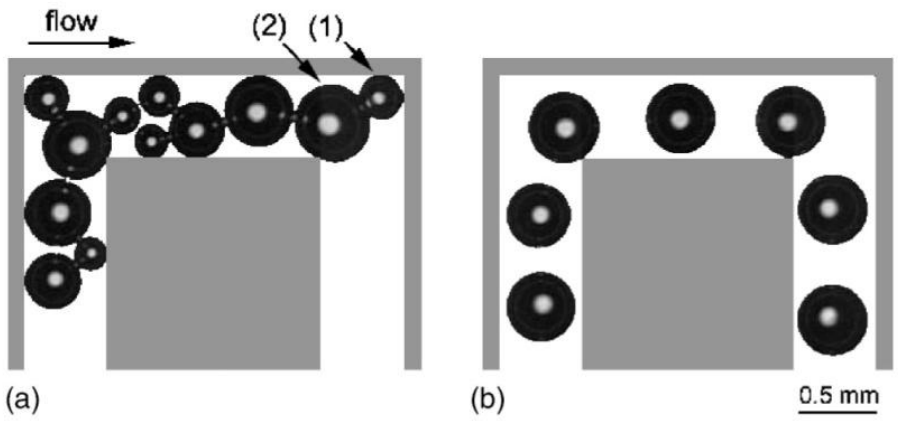

Fig. 1.7 Image of bubbly flow in a sharp return. [27] (a) low liquid velocity, (1) Small bubble trapped in the sharp corner. (2) Other bubbles become trapped as a chain reaction. (b) high liquid velocity.

1.3.2 Slug flow:

Slug flow (also known as plug flow, segmented flow, bubble train flow, wedging flow or Taylor flow) is the major and most common flow pattern that being studied extensively by many researchers [9 27 4]. Typical observation for this pattern is elongated bubbles span most of the channel cross-section [32], bubbles length can often reach several times of the channel diameter. In

this pattern, liquid slugs separate the gas bubbles while a liquid film may form between the bubbles and wall. Gunther *et al* [9] observed that recirculation happens in the liquid slug between bubbles, such recirculation would significantly improve microscale liquid mixing. This pattern exists at low gas superficial velocities in the entire range of liquid superficial velocities, as shown in Fig.1.5. In some cases, the plug liquid can also contain small gas bubbles. [32 33]

1.3.3 Churn flow:

At high liquid velocity, small satellite bubbles appear at the rear of the gas slug, as the slug bubbles become unstable near their trailing end. This chaotic flow pattern is called as the churn flow. Cubaud and Ho [27] reported that within the laminar flow range of their investigation, churn flow was not as easily observed in microchannels as in larger channels.

1.3.4 Annular flow:

With the increasing gas superficial velocity, the increasing gas void fraction causes slug bubbles to merge and form the annular flow. This pattern is also sometimes divided as two separate patterns; one is the slug-annular flow, also known as the Taylor-annular flow [32], the other is annular flow. In both the annular pattern, the continuous gas core is surrounded by the liquid film. However, interfacial waves along the gas core are observed in the slug-annular pattern. Waves are composed of liquid rings travelling along the gas core. The liquid rings appear because it is too short to support a stable liquid bridge between two consecutive slug bubbles. The wave can propagate both upstream and downstream and its motion is random [27]. In the annular pattern, there is no liquid ring observed. Cubaud and Ho [27] have shown that the partial wall dewetting phenomenon occurs in this regime and liquid would be concentrated in the corners of the non-circular channels.

1.3.5 Dispersed flow:

From the annular flow, with further increase of liquid superficial velocity, small droplet would dispersed into the gas core, and in most cases liquid film also forms between the wall and gas core. Because the microchannel geometry limitation, such high velocity for the mixture is hard to achieve and thus dispersed pattern is not always observed.

Chapter 2

2. CO_2 diffusion in microchannels

Most of the previous research focused on the bubble breakup mechanism, the final bubble size and distribution. The gas phases in these experiments are either air or Nitrogen which are not strongly diffusive in water and many other liquid solutions. Diffusive gas, such as Carbon dioxide, can be used to achieve smaller size microbubbles. Only a few researchers has investigated diffusive bubbles in microchannel, J.Park [34] has proposed such a way to use gaseous CO2 bubbles dissolute in varying acidity liquid medium to produced smaller size CO2 bubbles a few seconds after break up. They mainly focused on the desired bubble size at the steady state. Our study mainly focuses on the dynamic of bubble diffusion in microchannels under the milli-second scale.

2.1 Experiment setup

The microchannels we used in our experiment are made of glass and silicon and are fabricated in a clean room environment. The four inlet channels are etched following standard lithography method[18]. Pyrex glass pieces are anodic bonded to the top and the bottom of the etched-through silicon channel. A fiber light is placed at the other side of the channel to provide light for high-speed imaging (up to 20,000 frames per second). Liquids are injected by syringe pump from both side channels at identical flow rate (Q_L). Bone dry CO_2 gas is supplied from a compressed gas tank; its pressure is adjustable with a miniature regulator (0-100 Psig). Gas flow rate (Q_G) is measured with gas volumetric flow meters (0-1.280 SCCM). Experiments in

different channels were performed with water, ethanol, methanol and high viscosity silicone oils. Experiment setups are shown in Fig.2.1 and Fig.2.2, Liquid viscosity and surface tension are listed in Table.2.1.

Fluid	v (cSt)	γ (mN m^{-1})
Water	1.004	72.80
Ethanol	1.361	22.10
Methanol	0.687	22.70
PDMS (1cSt)	1	17.40
PDMS (10cSt)	10	20.10
PDMS (100cSt)	100	20.90
PDMS (1000cSt)	1000	21.20

Table 2.1 Physical properties of the liquids used in the experiments: v, γ are the kinematic viscosity and surface tension respectively.

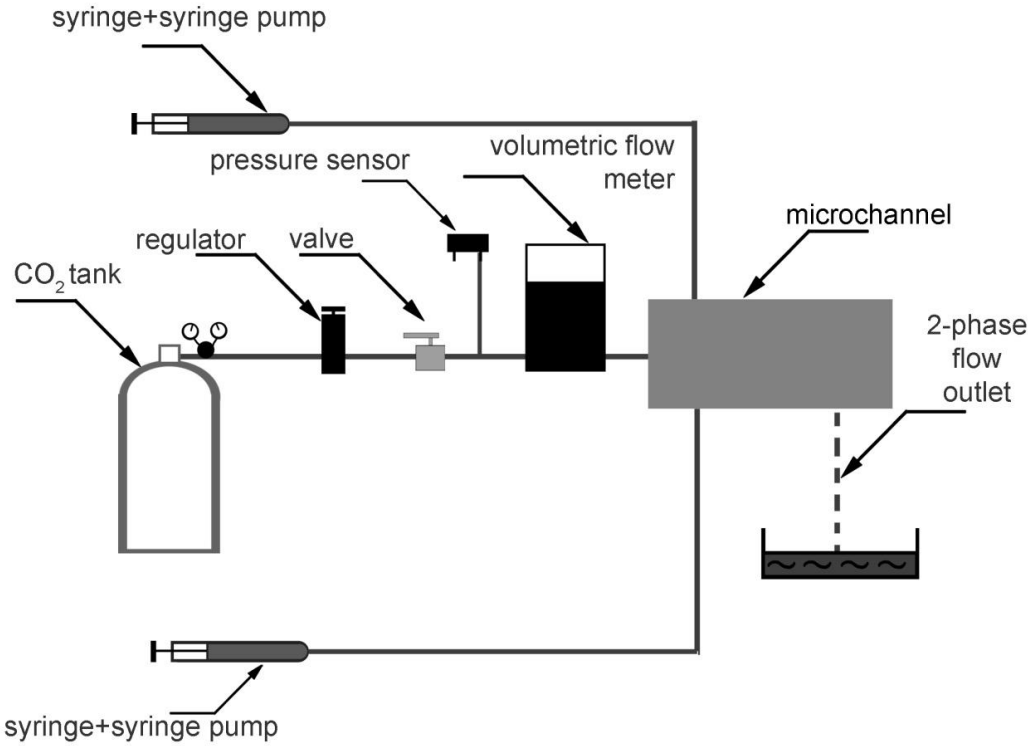

Fig. 2.1 Schematic of the experiment apparatus.

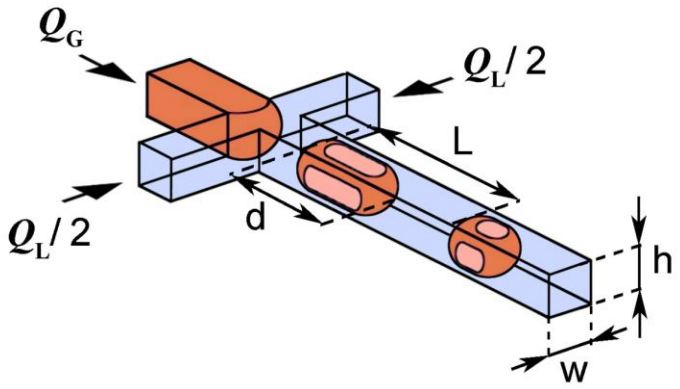

Fig. 2.2 3-D schematic view of the hydrodynamic focusing section. Q_L is the liquid flow rate; Q_G is the gas flow rate; *d* is the initial bubble length; *L* is the initial unit cell length between two consecutive bubbles; *w* is the channel width and *h* is the channel height.

We developed an image processing method (by using ImageJ, Matlab, Photoshop) which allows us to automatically acquire bubble's front and rear edge, and generate its spatial coordinate frame by frame. This technique is advantageous compared to manual scattered measurement. We calculate the bubble size evolution from the front and rear coordinates. This method gives us opportunity to explore the CO_2 diffusion instantaneously after the bubble break up. Differentiating the spatial coordinates with time, we calculate bubble's rear and front velocity evolution along the channel.

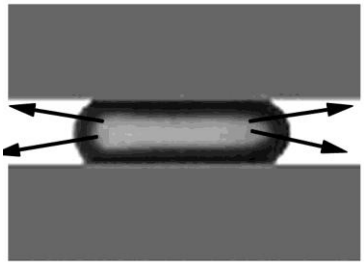

Fig. 2.3 Illustration of the gas diffusion through cap interfaces

2.2 CO2 bubbles in low viscosity liquids.

In this section we experimentally investigate the CO_2 bubbles formation, diffusion dynamics in low viscosity liquids (Water, Ethanol and Methanol).

2.2.1 Bubbles formation.

Previous study [18] has shown that homogenous liquid fraction $\alpha_L = Q_L / (Q_L + Q_G)$ is a key parameter to characterize the initial bubble size in square channel, as $d = h\ \alpha_L^{-1}$.

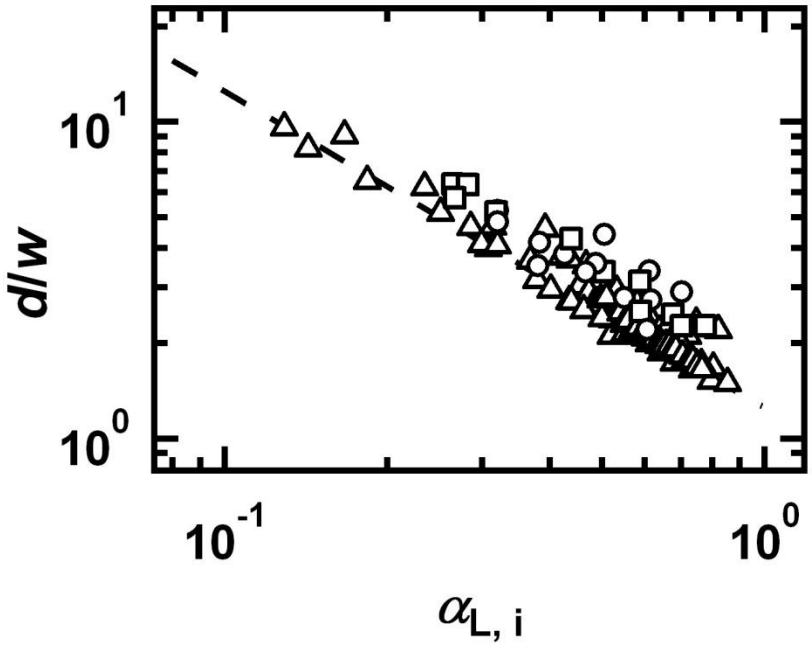

Fig. 2.4 Experiment results on initial bubble length d as a function of homogeneous liquid fraction α_L. CO_2/water (△), pressure range (17psia-25psia); CO_2/ethanol (○), pressure range(16psia-18psia); CO_2/methanol (□), pressure range(16psia-18psia); Dashed-line: $d/w = C\ \alpha_L^{-1}$,C= 1.25

In Fig.2.4, we plotted the bubble length d, normalized by channel width w, as a function of the homogenous liquid fraction α_L. Given the case that our channel is 100 μm × 80 μm, we

modified the previous expression of initial bubble size with a cross section aspect ratio C defined as h/w, that is

$$d/w = C\ \alpha_L^{-1} \qquad (2\text{-}1)$$

This empirical expression can be analytically deduced [18]. For liquid fractions $\alpha_L > 0.1$ ($Q_G/Q_L < 9$) and given the minimum dynamic viscosity contrast between liquid solution and CO_2 is around 36 ($\eta_L / \eta_G \sim 36$), the pressure gradient generated by the liquid flow ($\nabla P_L = A\eta_L Q_L / w^4$, with $A=28.43$) at the intersection is much larger (at least by a factor of 3) than the one generated by the cylindrical gas flow($\nabla P_G = 128\eta_G Q_G / \pi w^4$). Under these conditions and given the cylindrical shape of the gas thread, we can reasonably assume that the resistance offered by the gas for the liquid to flow across the intersection is negligible. Therefore, the time T necessary for the liquid to pinch the core gas bubble can be estimated by $T = w/J_L = wh^2 / Q_L$ (where J_L is the liquid superficial pinching velocity, since the pinching area expand at the liquid gas interface, we defined $J_L = Q_L / h^2$ instead of the cross section area wh). The bubble length d is proportional to the pinching time T and the average bubble velocity $J_G = (Q_L + Q_G)/(wh)$ in a rectangular channel, so we can estimate $d = J_G T$.

In Equation (2-1) we neglect the gas pressure's influence on the initial bubble size, based on the assumption that gas pressure is large enough to push the bubble to move down stream. However if the gas pressure is extremely low, the gas thread can be displaced back to the central channel. At a relatively low gas pressure range (16-18psia), due to the competition of gas and liquid pressure, the bubble generation time are longer than at higher pressure(18+psia), which renders our data at low gas pressure in Fig.2.4.to lay on top of the predication curve.

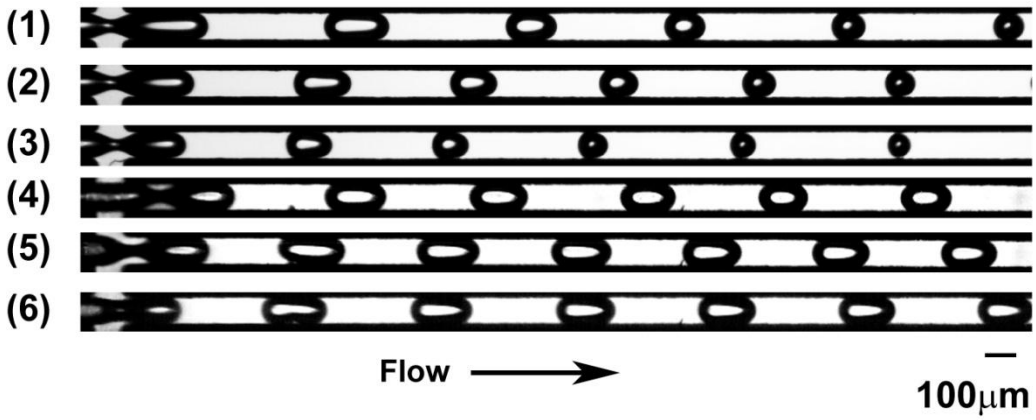

Fig. 2.5 Bubble formation at different gas pressure, similar liquid fraction,in water and ethanol. ;(1)Ethanol, P_G = 16psia, α_L = 0.612;(2) Ethanol, P_G = 17psia, α_L = 0.616;(3) Ethanol, P_G = 18psia, α_L = 0.612; (4)Water, P_G = 17psia, α_L = 0.571;(5) Water, P_G = 19psia, α_L = 0.581;(6) Water, P_G = 23psia, α_L = 0.578.

From Fig.2.5, due to strong CO_2 absorption in ethanol, we clearly found that with the increase of gas pressure, the initial bubble size reduces considerably. In water, as the gas diffusion process is much slower compared to ethanol, we found that the break up point was pushed into the central channel as we lowered the gas pressure, which means that the liquid thread is not pinch through the gas thread orthogonally. Thus the pinching speed is slower, and the pinching time is extended to generate bigger bubbles than our prediction. In ethanol and methanol, there are no significant shifts of the breakup position, however, due to the significant quicker CO_2 diffusion in ethanol and methanol, and since the gas solubility increased with pressure according to Henry's law, we can assume that gas diffusion has already processed before the bubble break up, and thus when we increased gas pressure, initial bubble size after break up would be reduced.

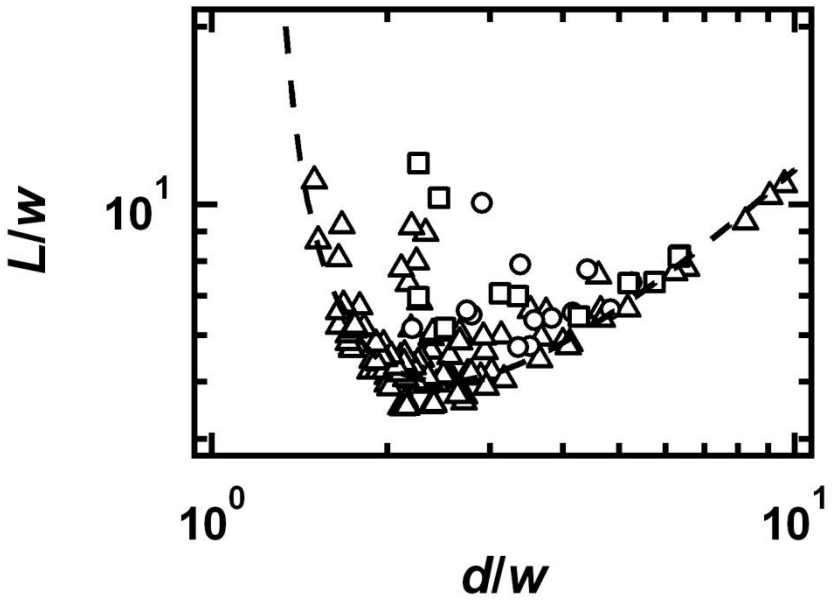

Fig. 2.6 Evolution of the distance L between bubbles as a function of bubble length d. CO_2/water (△), CO_2/ethanol (○), CO_2/methanol (□).Dashed-line: $L/w = (d/w)^2/(d/w-C)$,C=1.25.

Another important parameter to characterize bubbles formation is the bubble distribution, customizable using the distance L between the bubbles as shown in Fig 2.2. We used a first order approximation which neglects the bubble curvature, as well as the liquid flowing in the corner and in the thin film. By doing so, the bubble shape can be assumed as a rectangular plug of volume dwh. Along with the plug approximation, volume conservation allows estimating the distance L between bubbles by writing $1-\alpha_L = d/L$ combined with Eq.(2-1). The distance L between bubbles can be expressed as a function of the bubble length d, $L/w = (d/w)^2 / (d/w-C)$.As can be seen in Fig.2.6, experimental data in water follows our predication, while in methanol and ethanol, L/w lies top of the curve. That is because in methanol and ethanol, the CO_2 absorption rate is much faster than in water, the previously formed bubble has dissolved into the solvent before the forming one break up, which means the liquid plug between bubbles are longer than usual. Assuming the initial bubbles size is fixed, and the initial liquid plugs are extended, thus the distance L is larger than our prediction.

2.2.2 Gas diffusion.

Our microfluidic system permits the exploration of very short time scales (~1ms). Using conventional apparatus, it is very difficult to access regime where the CO2 concentration in the liquid is minimal (i.e., corresponding to the air).

Similar to heat transfer, diffusion rate is enhanced at the microscale due to the large area-to-volume ratio. Here, we investigate the dynamics of gas diffusion in liquids in segmented microflows. This flow configuration is particularly advantageous because the enhanced mixing due to the recirculation motion associated with the liquid plugs [35] tends to homogenize the concentration profile of dissolved gas in the bulk liquid medium. Hence, "sharp" concentration gradients are maintained between the interface and the bulk liquid leading to a very fast gas impregnation process. In addition, the large pressure associated to small-scale flows has a positive effect on the process since the solubility increased with pressure according to Henry's law.

We compared the time evolution of normalized bubble lengths *d/w* for a fixed gas inlet pressure, as shown in Fig.2.7. Although the homogenous liquid fraction α_L varies, the evolution curves are generally paralleled with each other, which indicate that the bubble shrink dynamic is independent with α_L. In Fig.2.8, we compared the bubbles time evolution for a fixed initial bubble size, and found that the increase gas pressure accelerate the diffusion process.

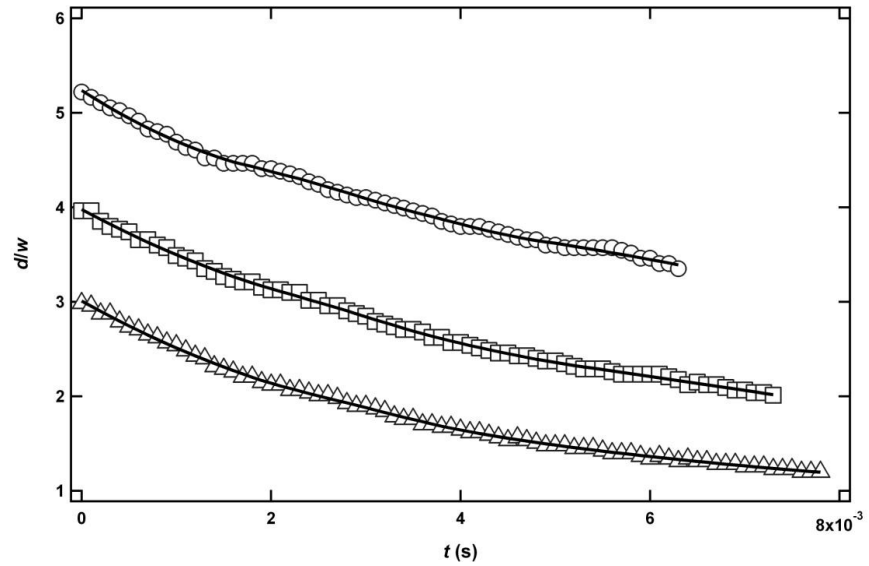

Fig. 2.7 Evolution of normalized bubble lengths d/w as a function of time for the fluid pair CO_2/ethanol. α_L =0.32 (○), α_L =0.43 (□), α_L =0.55 (△). Fixed inlet pressure $P_G \approx 17$ Psia (curves are parallel).

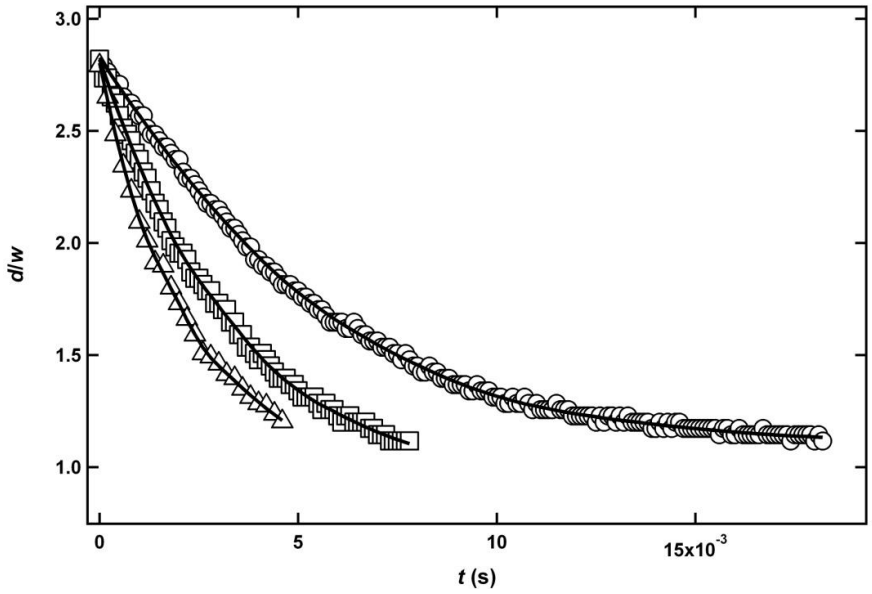

Fig. 2.8 Evolution of normalized bubble lengths d/w as a function of time for the fluid pair CO_2/ethanol. Fixed initial bubble length $d_0/w \approx 2.8$, for $P_G \approx 16$ Psia (○), 17 Psia (□), and 18 Psia (△). (the rate of diffusion increase with pressure)

The bubble length can be expressed as $d(t)/w = d_0/w - f(t)$.

We plot $f(t) = d_0/w - d(t)/w$ as a function of t and we do not find any significant change in the function for different initial bubble size d_0 [Fig. 2.9]. Indeed, for a given fluid pair at fixed temperature, the function f is experimentally found to depend only on the initial pressure P. For short period of time, the bubble is in fast diffusion mode because the concentration gradient is not well established. We use the dimensional time t rather than the dimensionless mixing time-scale t/τ with $\tau = hw/D$. We calculated τ in our system and the following values were obtained τ = 5.98 seconds for water, τ = 2.89 seconds for ethanol, and τ = 1.24 seconds for methanol. These values are in the order of 1 second and therefore do not yield significant insight particularly in the context of our experiments in the millisecond range. The use of the diffusion coefficient D alone is insufficient for describing liquid/gas diffusion process.

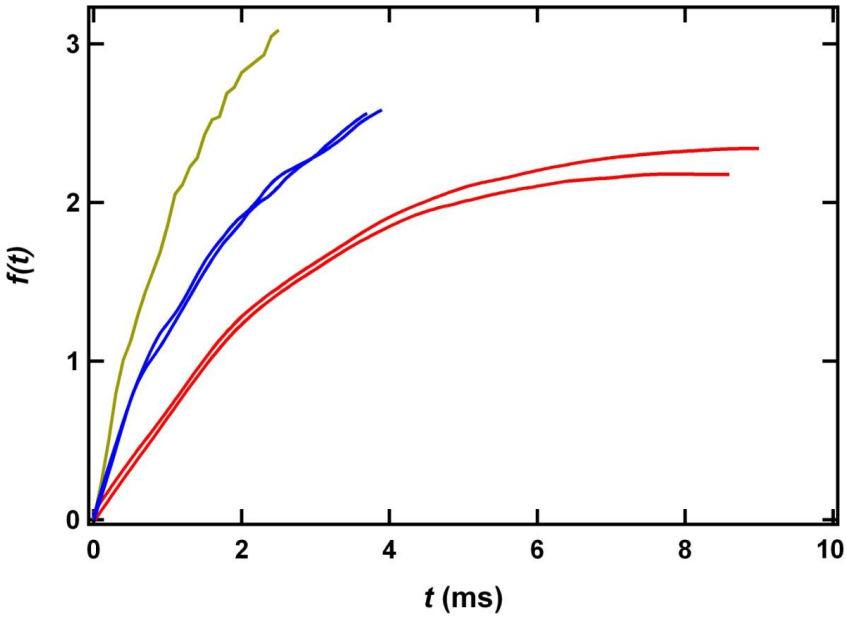

Fig. 2.9 Evolution of the function f as a function of time for the fluid pair CO_2/methanol. f(t) is essentially dependent of P_G. 16Psia (Red), 17Psia (Blue), 18Psia (Yellow).

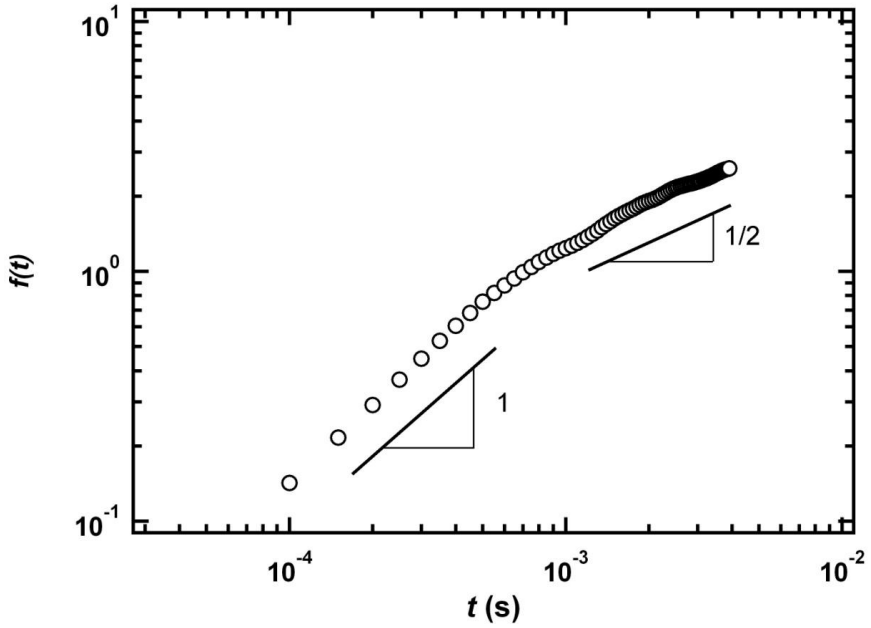

Fig. 2.10 Evolution of the function f as a function of time for the fluid pair CO_2/methanol. Bubble diffuse with $f \sim t$ (fast-diffusion mode) for initial contact and $f \sim t^{0.5}$ for long periods of time (normal-diffusion mode).

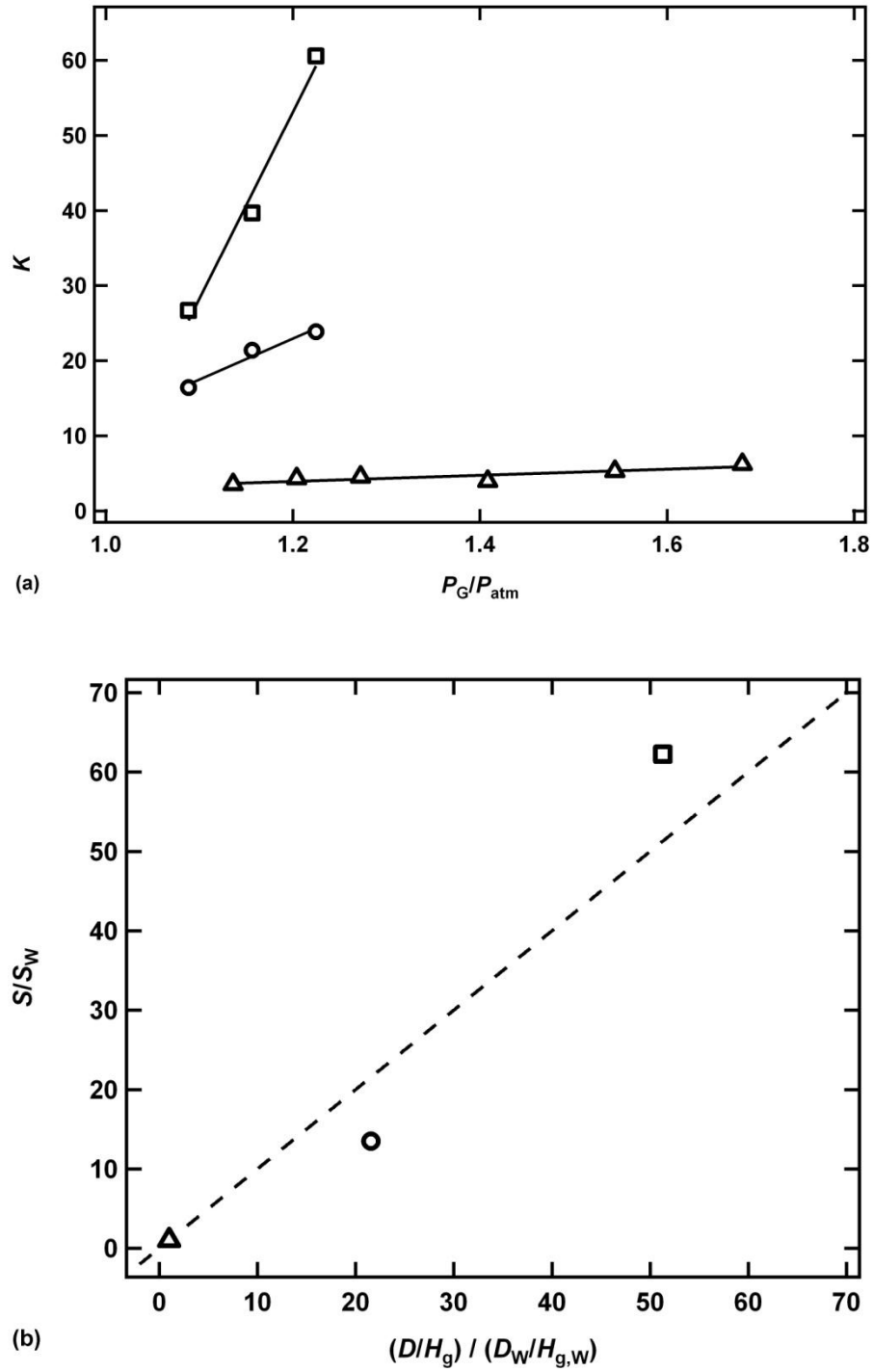

Fig. 2.3 Rate of diffusion for different fluid pairs: CO_2/water (△), CO_2/ethanol (○), CO_2/methanol (□). (a) Evolution of the prefactor k as a function of normalized pressure (b) Relative effective diffusion rate vs. model prediction from Eq. (3-4). Dashed-line: $S/S_w = (D/H_g)/(D_W/H_{g,W})$

Over the range of pressure investigated, we fit $f(t)$ for the three fluid pairs with a power law $kt^{0.5}$, with k being a coefficient that depends on P and the fluid pair [Fig.2.11.(a)]. Hence, for relatively long intervals of time ($t > 10^{-3}$ s), the bubble length can be expressed as:

$$d(t)/w = d_0/w - kt^{1/2} \tag{2-2}$$

Experimentally, the coefficient k is found to be a linear function of $P^* = P/P_{atm}$ with the slope $k = SP^*$ and values $S_{water} = 4 \pm 1$, $S_{ethanol} = 54 \pm 10$, $S_{methanol} = 249 \pm 33$. This expression allows for estimating the evolution of the bubble size: $d/w = d_0/w - SP^*t^{1/2}$. Overall, the volume flow rate of diffusion $Q_{diff} \sim (dd/dt)wh \propto (SP/2)\ t^{-1/2}$ There is a wide variation of the "effective diffusion rate" S as a function of the liquid solvent.

For practical applications, it is important to know a priori the numerical value of S. Here, we develop a simple model that allows for predicting S based on the physicochemical properties of the fluid pair. We assume equilibrium between the gas and the liquid at the interface according to Henry's law $P = H_gC$, where H_g is the Henry constant, and C is the mass fraction concentration in the liquid at the interface. The diffusion of CO_2 in the liquid obeys the simple diffusion equation, i.e., Fick's Law: $J = -\rho D\nabla C$, where J is the mass diffusion flux, ρ is the mass density, D is the diffusion coefficient, and ∇C is the mass fraction concentration gradient[36]. For elongated bubbles in a compact channel, the quasi one-dimensional mass transfer occurs primarily across the two bubble ends: $J \sim Q_{diff}/(2wh)$. Since the CO_2 concentration in the bubble is constant and varies only in the liquid, the concentration gradient is assumed to scale as $\nabla C \sim C/w$. Therefore, based on Fick's law, we estimate $Q_{diff} \sim 2DCh$, which when combined with Henry's law yields: $Q_{diff}/(2hP) \sim D/H_g$. Since $Q_{diff} \propto SP/2$, one would expect proportionality between the effective rate of diffusion S and the ratio of the diffusion coefficient D to the Henry constant H_g, i.e.

$$S \sim D/H_g. \quad (2\text{-}3)$$

The ratio D/H_g is very small. Therefore, we plotted (D/H_g) with reference of water [Fig.2.11 (b)].

Following are the diffusion coefficients D and Henry's constants H_G used in this work. Although our experiments were performed around 20^0 C (293 K), most data are found at 25^0 C (298 K), therefore for consistency we use the later. In particular for comparing liquids, the relative difference between these values is more relevant that their absolute value

	Water	Ethanol	Methanol
D (m^2/s)	1.97×10^{-9} [37] 1.94×10^{-9} [38] 1.88×10^{-9} [39]	3.46×10^{-9} [40] 3.42×10^{-9} [37] 3.88×10^{-9} [41]	8.02×10^{-9} [42] 8.37×10^{-9} [41]
H_G (kPa) (298 K)	167085 [40]	16009 [43]	14500 [44]

Table 2.2 Diffusion coefficient and Henry's constant of liquids used in the experiment.

Given the large range variation in both D and H_g, we find the agreement relatively good. Our model allows for predicting the diffusive flow rate based on pressure P, diffusion coefficient D, and Henry constant H_g in microchannels.

2.2.3 Bubble velocity evolution

We also analyzed the spatiotemporal diagrams of bubble path by using numerical routines to extract the bubble front and rear velocity V_F and V_R, as plotted in Fig.2.12.We manage to measure the bubble front velocity before break up, which shows its velocity increases sharply at the very beginning of formation, the peak velocity is achieved just before the break up. The rear velocity V_R of a shrinking bubble is larger than the front velocity V_F. As the bubble flows downstream, V_R approach V_F, and eventually become the same which indicates that the bubble size reaches a steady state. In Fig.2.13, we plotted the evolution of gas void fraction α_G (using plug approximation as $\alpha_G = [(d\text{-}w)\, wh + 4/3\pi(w/2)^3]/Lwh$) as a function of time t compare to the predicted void fraction $\alpha_{G\ dif}$ calculated from $d(t)$. It is assumed that there is no appreciable change in the (partial) volume in the liquid when the gas is absorbed. Thus the gas void fraction would decrease accordingly with bubble shrinking dynamics

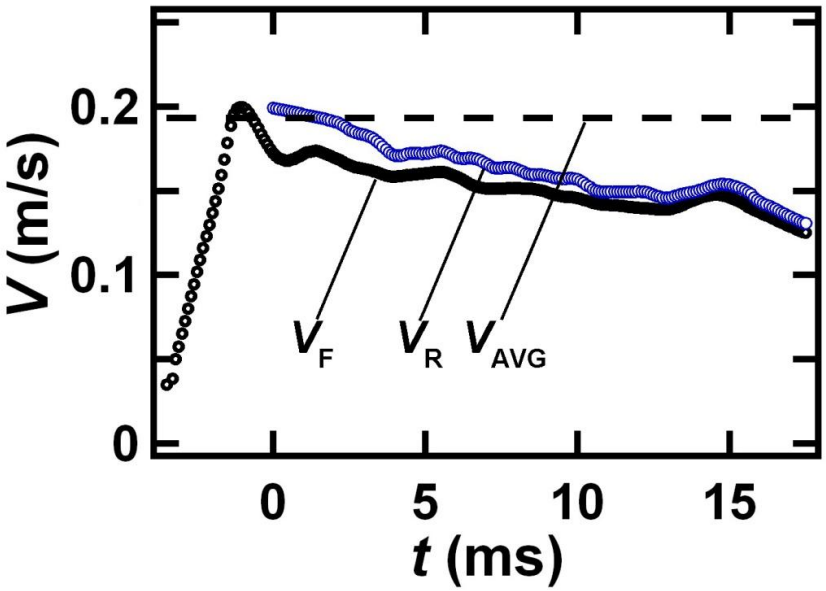

Fig. 2.4 Temporal evolution of bubble front velocity V_F and rear velocity V_R. (Ethanol, 16Psia, Q_G=49μL/min, Q_L=50 μL/min.),

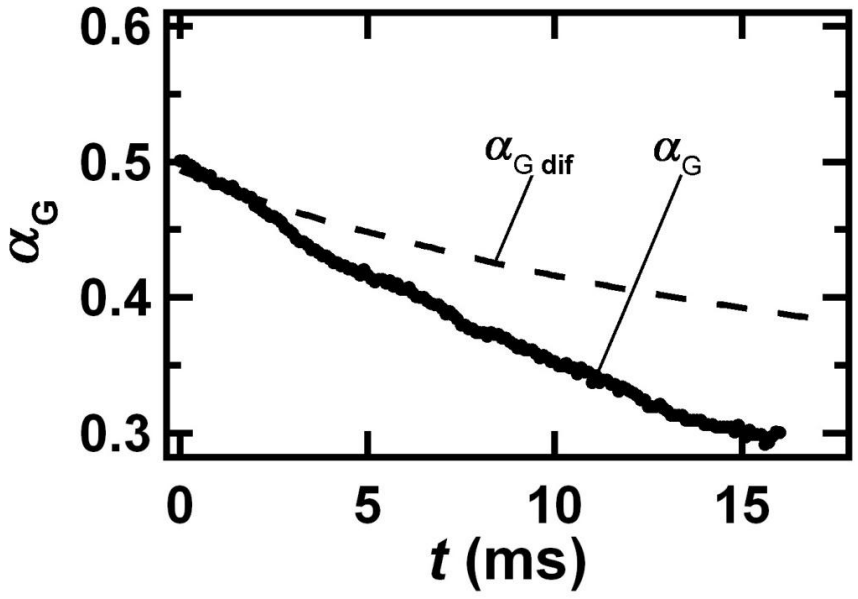

Fig. 2.5 Evolution of gas void fraction α_G compared with the calculated gas void fraction $\alpha_{G\ dif.}$ (Ethanol, 16Psia, Q_G=49μL/min, Q_L=50 μL/min.)

2.2.4 Bubble evolution at long serpentine channel

We follow the motion of CO_2 bubbles further downstream in a long serpentine channel, where monodispersed dilute bubbly flows are observed at certain flow rates, as shown in Fig.2.14. The smallest bubble diameter can be achieved is at the scale of 1/3 of the channel width (~30μm in our experiment).We then characterize the flow pattern in water as Fig.2.15. There are basically three flow region as: bubbly, slug and transition. At the transition region, a process of destabilization occurs when series of coalescence produces a large, slow leading bubble that collects the fast tiny bubbles on its trail. Although the velocity of elongated bubbles is comparable to the local average superficial velocity *V* of the flow, tiny spherical bubbles convected in the parabolic Poiseuille flows move faster than *V*, as shown in Fig.2.16.

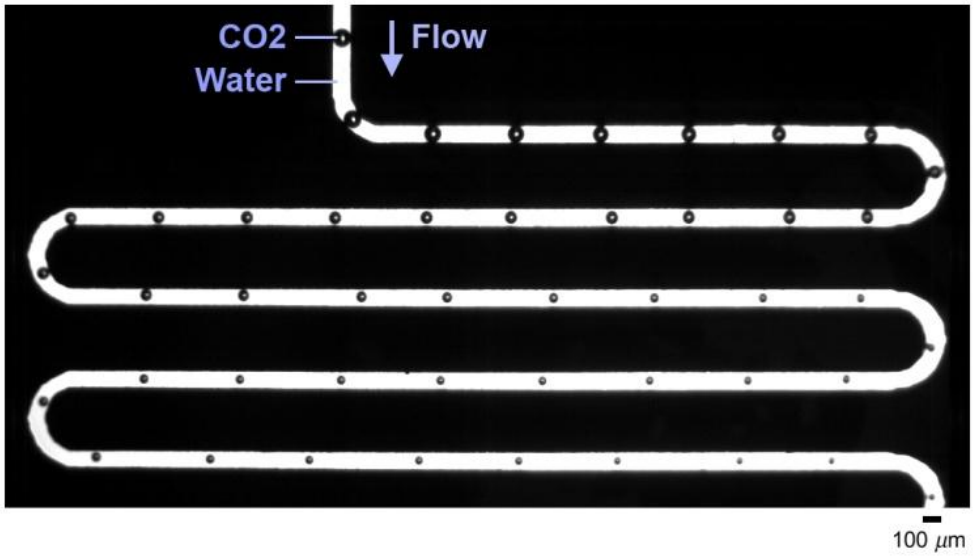

Fig. 2.6. Bubbly flows of carbon dioxide bubbles in water.

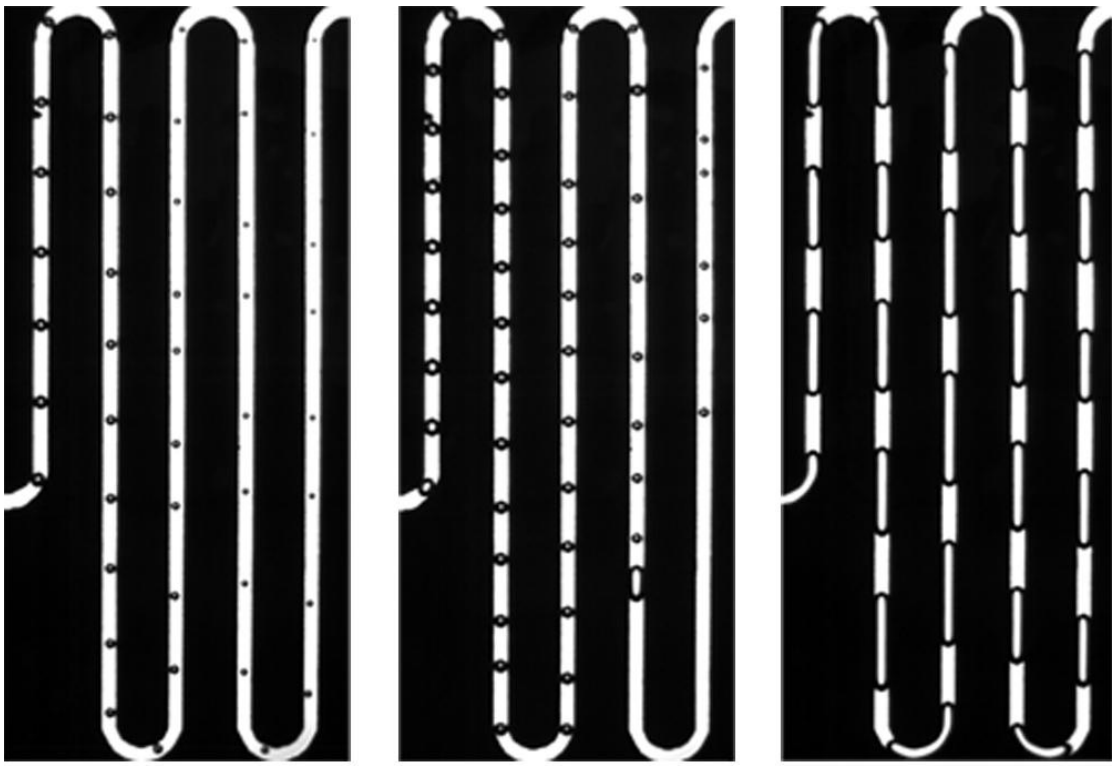

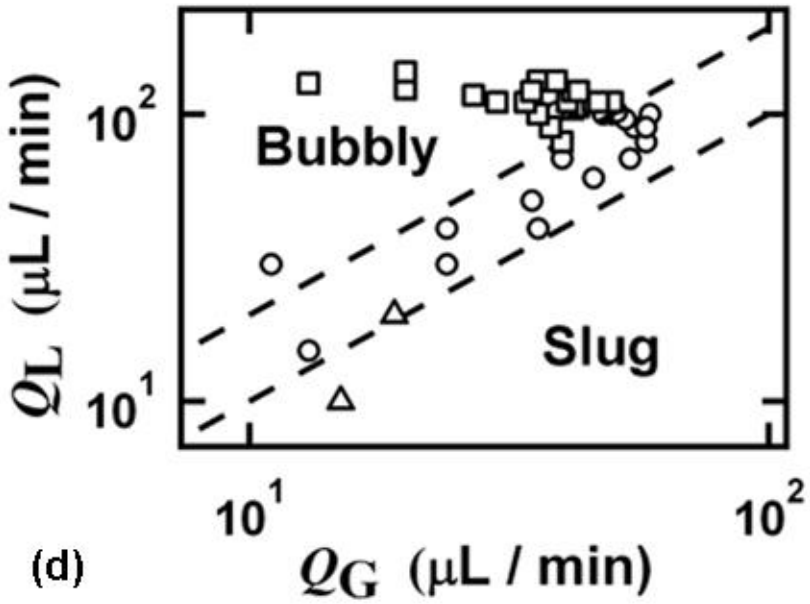

Fig. 2.7 Flow patterns in long serpentine microchannels. (a) Bubbly flow. (b) Transition flow. (c) Slug flow. (d) Flow pattern map.

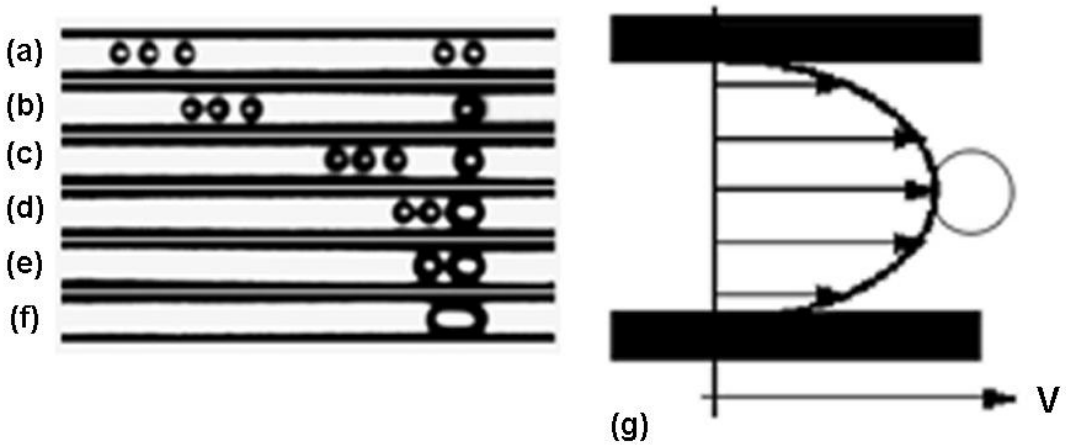

Fig. 2.8 Bubbles coalescence along long serpentine microchannels. (a)- (f) Sequence of coalescence between small bubbles in the reference frame of the leading bubble.(g) Schematic of the parabolic velocity profile.

2.3 Bubbles formation in high viscosity liquid

In this section we analyzed the carbon dioxide bubbles generation in high viscosity silicone oil (1-1000 cst). We measure the bubble width *d'* and the channel width *w*, and then calculate the liquid thickness δ by subtracting *d'* from *w*, as shown in Fig.2.17.

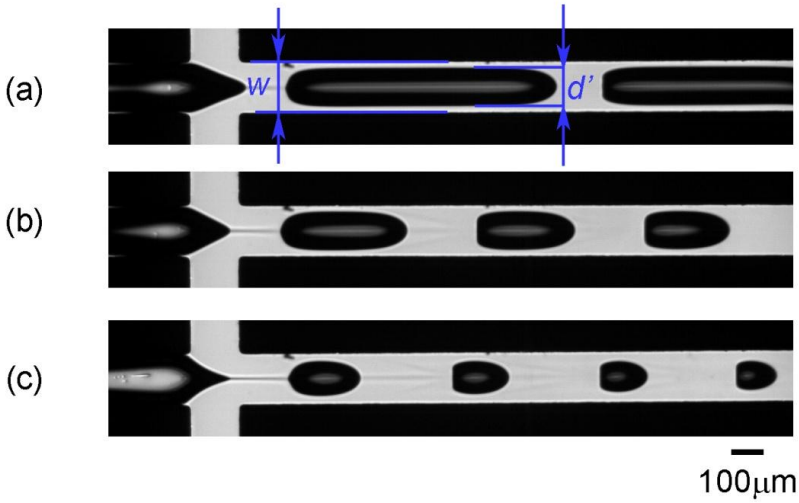

Fig. 2.9 Bubble formation in silicone oil. (a) 1000cst, P_G=50Psia, Q_G=83μL/min, Q_L=20μL/min. (b) 1000cst, P_G=50Psia, Q_G=47μL/min, Q_L=34μL/min. (c) 1000cst, P_G=61Psia, Q_G=40μL/min, Q_L=64μL/min.

We plot the dimensionless liquid thickness δ/w against the capillary number Ca. As shown in Fig.2.18, the dimensionless liquid thickness δ/w approaches 0.05 as the capillary number Ca decreases, which agrees well with Kolb and Cerro's result. [45] Kreutzer *et al* [31] correlated the dimensionless liquid thickness in square channel against capillary number as:

$$\delta/w=0.3-0.5 \exp(-2.25Ca^{0.445}) \qquad (2\text{-}4)$$

which is also plotted in Fig.2.18. Our experiment data agrees nicely with their prediction at the entire range of capillary number.

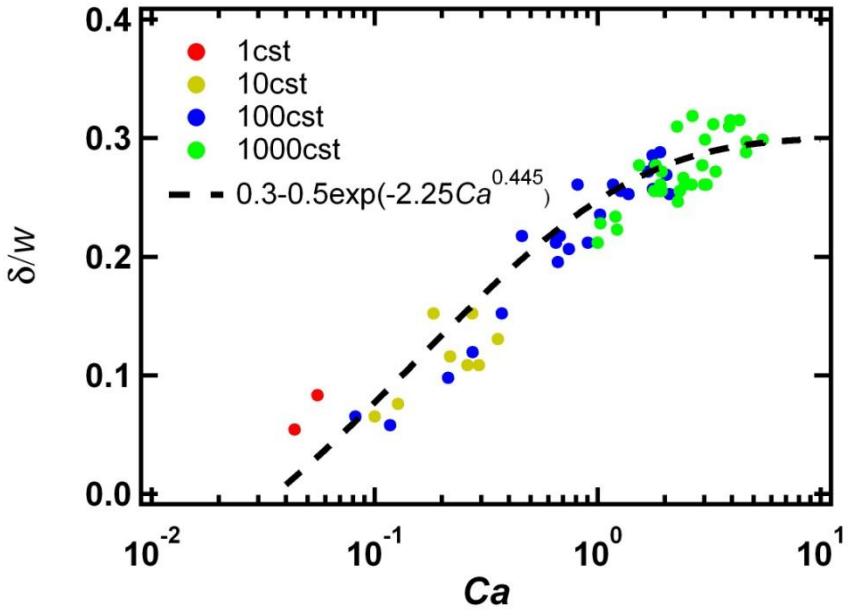

Fig. 2.10. Film thickness between elongated bubbles and microchannel wall, as a function of the capillary number Ca. Silicone oil with different viscosities: 1cst (Red), 10cst (Yellow), 100cst (Blue), 1000cst (Green).

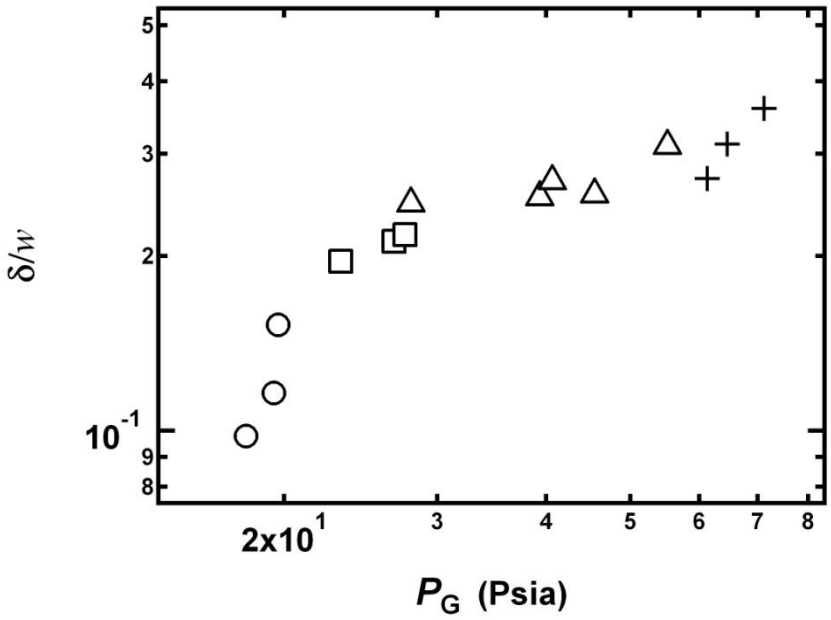

Fig. 2.11 Film thickness versus the gas pressure P_G for different capillary number group.Ca=0.2 (○), Ca=0.6 (□), Ca=2.0 (△), Ca=3.0 (+). The liquid thickness is proportional to the gas pressure.

In Fig.2.19, we plot the dimensionless liquid thickness δ/w against the gas pressure P_G. We found that for the same capillary number, the liquid thickness increase as the gas pressure increase, which agrees well with our experiment data at low viscosity liquid. The increased gas pressure accelerates the gas adsorption, and as the bubble size reduces in both axial and radial direction, its liquid film thickness increases.

Chapter 3

3. Carbon Dioxide cavitations in capillary.

In this section, we investigate the formation of CO_2 bubbles in carbonated water by depressurization along the microchannels. The bubbles cavitations are often seen in carbonated soft drinks. Before the bottle or can is opened, the gas above the drink is almost pure carbon dioxide at a pressure slightly higher than atmospheric pressure. The drink itself contains dissolved carbon dioxide. When the bottle or can is opened, some of this gas escapes, giving the characteristic hiss. Because the pressure above the liquid is now lower, some of the dissolved carbon dioxide comes out of solution as bubbles. Vapor bubbles formation in microchannel has been studied by a few researchers [46] [47],but they mainly used local heating rather than depressurizing to generate vapor bubbles.

3.1 Experiment Apparatus

Fig.3.1. shows the schematic of the experiment apparatus, in which we visualize the CO_2 bubble cavitations from saturated CO_2-water mixture in capillary tube. We construct a water tank with two sealed outlets; the gas inlet is above the water level, while the liquid outlet is under the water level. Next we input a magnetic stirrer (Sigma-Aldrich Spinbar® Disposable Magnetic Stirring Bars 2 in × 5/16 in) into water, seal the tank. Residual air is removed by introducing a vacuum bypass. After the residue air removal, the bypass valve is closed, while the gas inlet valve is opened. Bone dry CO_2 is injected from pressurized tank, gas pressure can be adjusted by

using the miniature pressure regulator (Bellofram Corp. Type91 Reg.0-100 Psig); Inlet gas pressure is measured by pressure sensor (Honeywell.ASCX100DN) and recorded by using the data acquisition card (National Instrument CB-37F-LP) and LABVIEW. To enhance the CO_2 mixing with water, we use the Sigma-Aldrich ceramic top hot plate stirrer (Ika Works. Msc Basic S47) to stir the magnetic Spinbar at 400RPM. The system is allowed to reach a saturation state (10 minutes). We then stop the stirrer, turn on the liquid outlet valve, keep the gas inlet valve open, allow the liquid mixture to flow downstream to the capillary tube(Wale Apparatus Co. Vitrotube® 0.5 mm × 0.05mm) connected by using Upchurch tubing (1/16 in diameter). The carbonate water pressure is also measured and recorded by using secondary pressure sensor. The capillary outlet is permitted to vent directly into the atmosphere. A high-speed camera (Redlake Motion Xtra HG-100K) is connected with inverted microscope (Accu-Scope® 3035 Microscope Series) to allow flow analysis. As the capillary is transparent, the light source (Fiber Lite Mi-152 High Intensity Illuminator) is placed on top of the microscope.

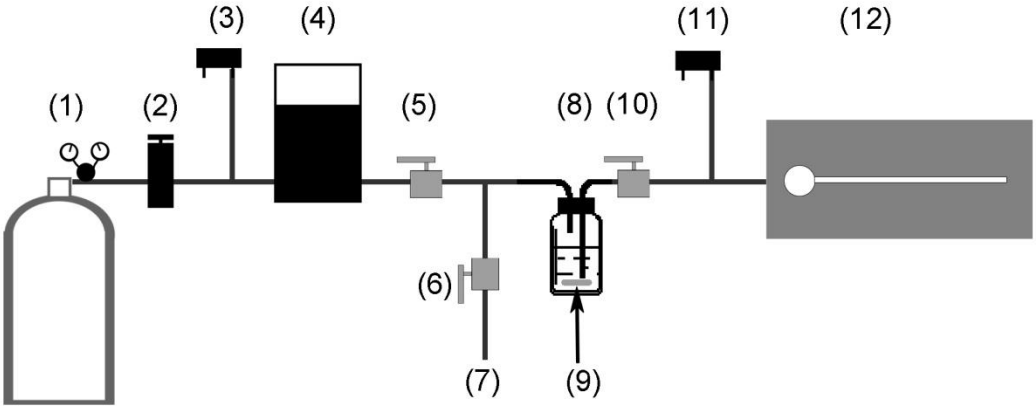

Fig. 3.1 Schematic of the experiment apparatus: (1)Gas tank, (2)Miniature regulator, (3)Inlet pressure sensor, (4) Gas flow meter, (5) Inlet valve,(6) Bypass valve, (7) Vacuum, (8) Sealed reservoir, (9) Spin bar, (10) Outlet valve, (11) Outlet pressure sensor, (12) Capillary tube.

3.2 Result and discussion.

Fig.3.2 shows the bubble cavitation formation in the 0.5 mm × 0.05mm capillary, the time scale for the bubble formation is about 1s while the flow time scale can be calculated as: $\tau = w/U \sim w/(Q_{TOT}/w^2) \sim 0.01$s. There are around two magnitude difference between the bubble cavitation velocity and the flow velocity.

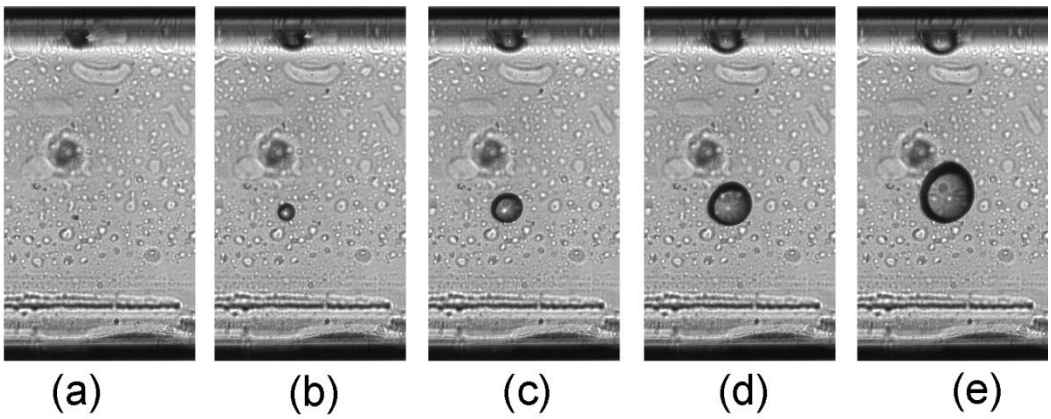

Fig. 3.2 Time series of the bubble growth at the square capillary wall. (a) t=0 s.(b) t=0.5 s,(c) t=1.0 s, (d) t= 1.5 s, (e) t= 2.0 s.

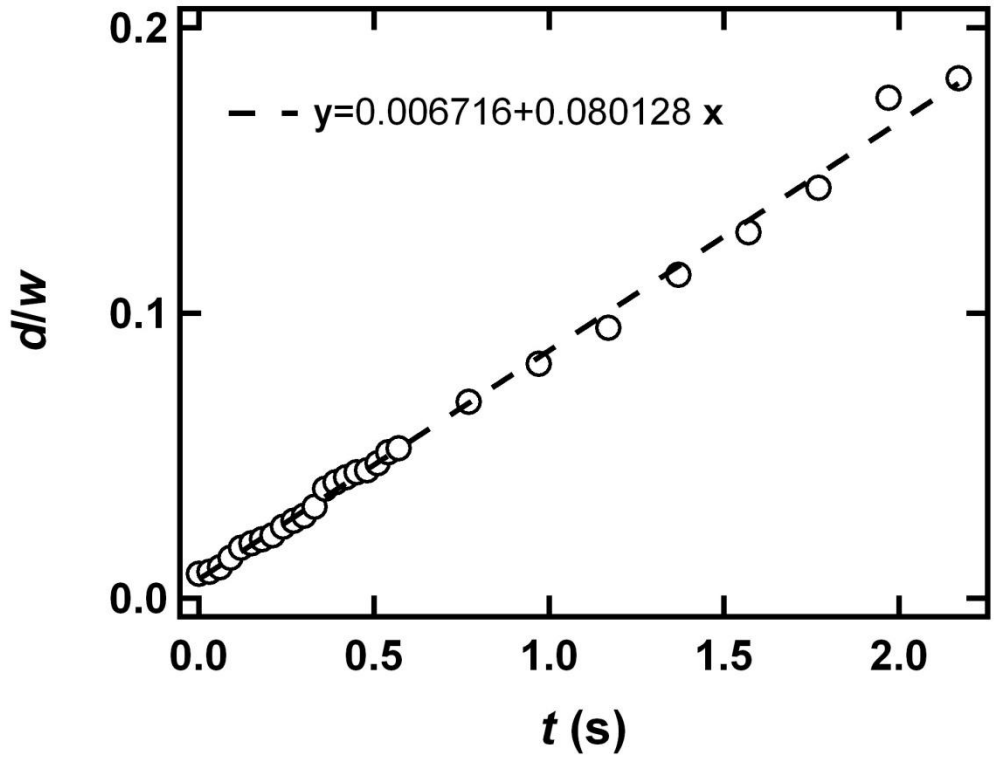

Fig. 3.3 Time evolution of the nondimensionalized bubble diameter

In Fig.3.3, we plot the nondimensionalized bubble diameter against time; we found that the bubble growth is linearly dependant to the time as: $d/w \sim t$, which is similar to the scaling law of initial gas diffusion we discussed in chapter 2.

Chapter 4

4. Co-flowing capillary tip fabrication

We choose the Borosilicate Glass capillary (Sutter Instrument.BF150-86-10) with 1.5 mm outer diameter, 0.86 mm inner diameter. We insert the capillary into the micropipette puller (Sutter Instrument. P-97) to run a ramp test first to determine the material property of capillary, Test result are shown in Table.4.1.(a). According to the instruction manual, in order to obtain a long taper and small pipette tip diameter, we choose the FB245B box filament to hold the capillary and adjust the control parameter as shown in Table.4.1. (b).to pull the capillary. The sample pipette has a 16mm taper with a 6μm tip diameter; Fig.4.1 shows the pipette diameter profile along the axial direction.

	PRESSURE	HEAT	PULL	VELOCITY	TIME
(a)	\	712	\	\	\
(b)	200	732	100	120	200

Table 4.1 (a) Ramp test result of the BF150-86-10 capillary tube. (b) Selected control parameter for the P-97 micropipette puller.

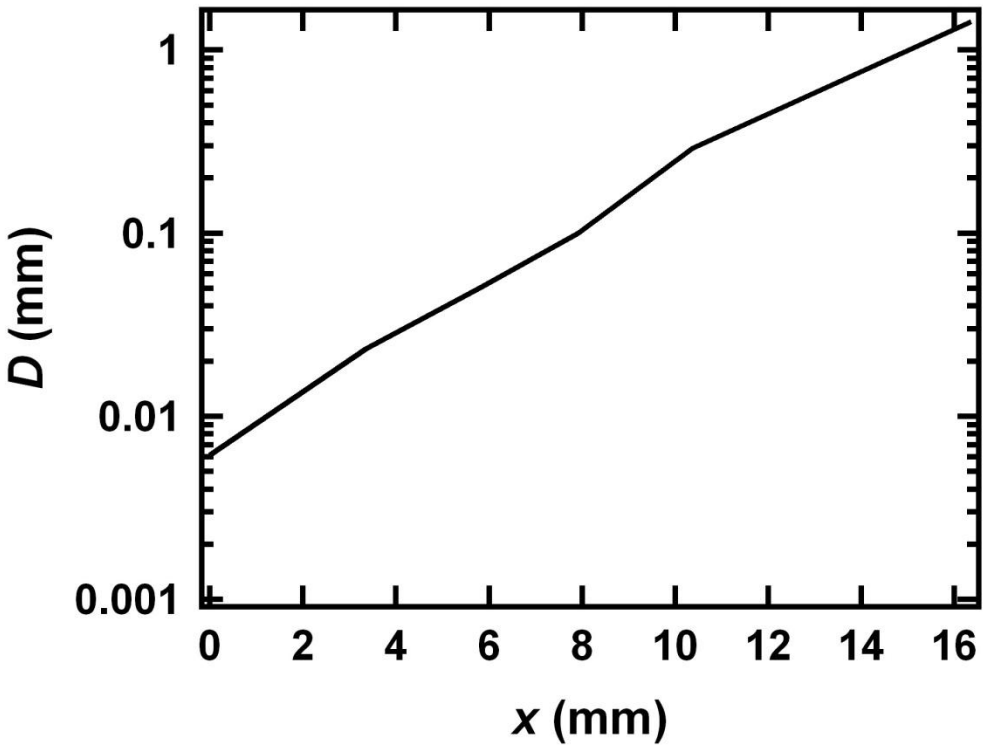

Fig. 4.1 Profile of the micropipette diameter along its axial direction. The maximum taper length is 16mm.

Next we use the 3-axial stage (Future Digital Scientific Corp. Contact Angle System RCA) to insert the micropipette into a 500μm×500μm square capillary tube (WALE APPARATUS CO.VITROTUBE® 0.5 mm × 0.5mm).Installation scene is shown in Fig.4.2. We first adhere the capillary to the microscope slides (J.Melvin Freed Brand. 75mm × 25mm) at a proper position where we can insert the micro pipette by adjusting the micro stage. The micro pipette position inside the capillary is monitored by camera.

According to the micro pipette diameter profile, the inserted taper length would be around 11mm, where the micro pipette diameter matches the square channel diameter, as shown

in Fig.4.3.

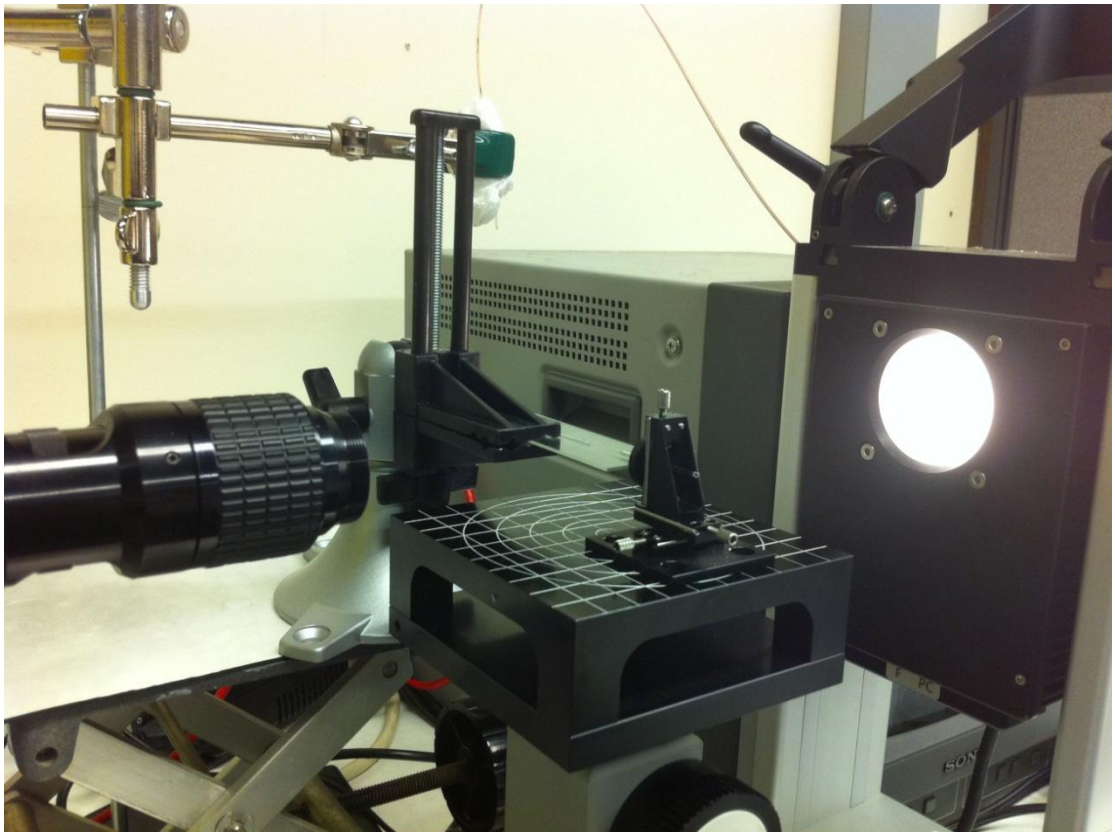

Fig. 4.2 Experiment setup for the micropipette installation.

Fig. 4.3 Schematic view of the center injection capillary layout. The cross section view shows its self-centered geometry.

Although ideally this method would automatically center the micro pipette inside the square channel, it is still a hard task to precisely control the three dimensional centering of the injection needle due to the fact that any small vibration would shift the contact line between the inner and

outer capillary. Because after the insertion of micro pipette, we still need to use peek tubing (Upchurch Scientific) to connect the gas inlet and liquid inlet, we also need to glue the connection cap, such vibration is inevitable. The asymmetrical insertion of micro pipette leads to another difficulty when observing the bubble generation under the microscope. It is relatively hard to focus the tip and wall at the same time due to the asymmetrical tip position in the vertical plate, thus the image quality is comprised.

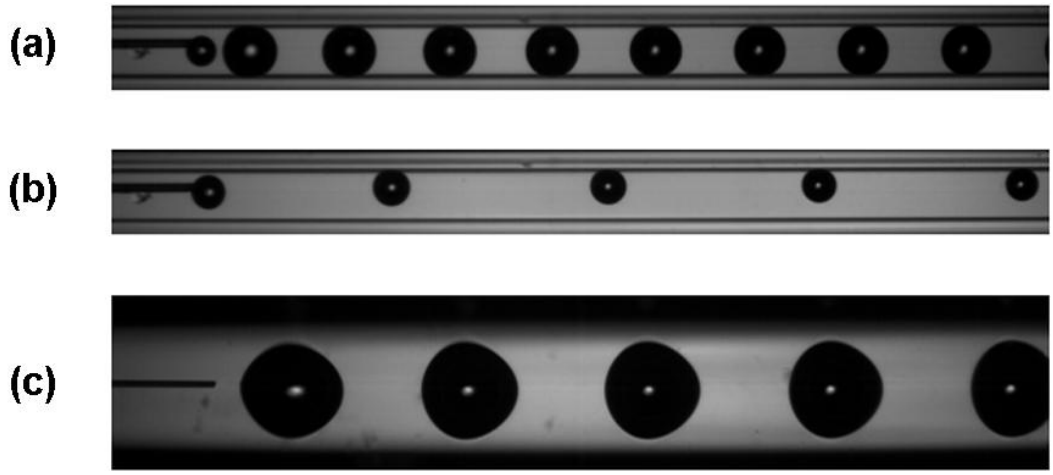

Fig. 4.4 CO2 bubble formation by using the co-flowing capillary tip. (a) Symmetric bubbles formation. (b) Non-symmetric bubbles formation. (c) Focal planes not on the same level.

Chapter 5

5. Conclusion and Future Work

In this thesis, parametric studies on the mass transfer during CO_2 absorption into water, ethanol, methanol and silicone oil under slug flow in microchannels are carried out experimentally. We show that the initial bubble size is determined by the liquid fraction and channel geometry, while the CO_2 diffusion are determined by the gas pressure and liquid solution. We found that the diffusion rate is related to the Henry's constant and proposed a simple model for bubble diffusion rate in microchannels. The reduction of the gas void fraction α_G evolution along the flow direction and the transformation of segmented flows into dilute bubbly flows was observed and predicted. In high viscosity liquids, we measured that the liquid film thickness is proportional to the capillary number and the gas pressure. We also constructed experimental setup for investigating the CO2 cavitation in microchannels. A linear time dependence of bubble growth from depressurization is observed. In addition, we proposed the fabrication procedure of co-flowing capillary tip and listed its current limitations.

In the future, we would like to implement a pressurized outlet to decouple the gas pressure and the flow velocity. It is also hoped to adapt CFD method to model our experiment results.

Bibliography

1. H. Stone, A. and Kim.S, AlChE.J **47** (6), 1250-1254 (2001).

2. Zhao.Y., O. Hemminger and S. F. Liang, Chem.Eng.Sci **62**, 7172-7183 (2007).

3. S. Irandoust, S. Ertle and B. Andersson, Can.J.Chem.Eng **70** (1), 115-119 (1992).

4. J. M. van Baten and R. Krishna, Chem.Eng.Sci **59**, 2535-2545 (2004).

5. W. Salman, A. Garvriilidis and P. Angeli, AlChE.J **53** (6), 1413-1428 (2007).

6. N. Shao, A. Garvriilidis and P. Angeli, J.Chem.Eng. **160**, 873-881 (2010).

7. Ajaev.V.S and Homsy.G.M, Annu.Rev.Fluid Mech **38**, 277-307 (2006).

8. S. Khan, A. Gunther, M. Schmidt and K. Jensen, Langmuir **20** (8604-8611) (2004).

9. A. Gunther, S. Khan, M. Thalmann, F. Trachsel and K. Jensen, Lab Chip **4**, 278-286 (2004).

10. A. Gunther, M. Jhunjhunwala, M. Thalmann, M. Schmidt and K. Jensen, Langmuir **21** (1547-1555) (2005).

11. Thorsen.T., Roberts.R.W., Arnold.F.H. and Quake.S.R., Phys. Rev. Lett **86**, 4163-4166 (2001).

12. Christopher.G.F and Anna.S.L, J.Phys.D: Appl.Phys **40**, 319-336 (2007).

13. P. Garstecki, M. Fuerstman, J., H. Stone, A. and G. Whitesides, M., Lab Chip **6**, 437-446 (2006).

14. T. Fu, Y. Ma, D. Funfschilling, C. Zhu and H. Li, Z., Chem.Eng.Sci **65**, 3739-3748 (2010).

15. Husny.J. and Cooper-White.J.J., Journal of Non-Newtonian Fluid Mechanics **137** (1-3), 121-136 (2006).

16. J. H. Xu, Li.S.W, G. G. Chen and G. S. Luo, AlChE.J **52** (6), 2254-2259 (2006).

17. Knight.J.B., Vishwanath.A., Brody.J.P. and Austin.R.H., Phys. Rev. Lett **80** (17), 3863-3866 (1998).

18. T. Cubaud, M. Tatineni, X. Zhong and C.-M. Ho, Phys. Rev. E **72**, 037302 (2005).

19. Ganan-Calvo.A.M., Phys. Rev. Lett **80**, 285-288 (1998).

20. Anna.S.L, Bontoux.N. and H. Stone, A., Appl.Phys.Lett. **82**, 364-366 (2003).

21. Jensen.M.J., H. Stone, A. and Bruus.H., Phys.Fluids **18**, 077103 (2006).

22. P. Garstecki, Gitlin.I., DiLuzio.W., G. Whitesides, M., E. Kumacheva and H. Stone, A., Appl.Phys.Rev.Lett. **85** (13), 2649-2651 (2004).

23. B. Dollet, W. van Hoeve, J. P. Raven, P. Marmottant and M. Versluis, Phys. Rev. Lett **100**, 034504 (2008).

24. N. Dietrich, S. Poncin, N. Midoux and H. Li, Z., Langmuir **24**, 13904-13911 (2008).

25. Cramer.C, Fischer.P. and Windhab.E.J, Chem.Eng.Sci **59** 3045-3058 (2004).

26. Marin.A.G., Campo-Cortes.F. and Gordillo.J.M., Colloids and Surfaces A: Physicochem.Eng.Aspects **344**, 2-7 (2009).

27. T. Cubaud and C.-M. Ho, Phys.Fluids **16**, 4575 (2004).

28. Chung.P.M.-Y. and Kawaji.M., Int.J.Multiphase Flow **30** (7-8), 735-761 (2004).

29. Galbiati.L. and Andreini.P, Int.Commun.Heat Mass Transfer **21**, 461-468 (1994).

30. Thulasidas.T.C, Abraham.M.A and Cerro.R.L., Can.J.Chem.Eng **50** (2), 183-199 (1995).

31. Kreutzer.M.T, Kapteijn.F, Moulijn.J.A and Heiszwolf.J.J, Chem.Eng.Sci **60**, 5895-5916 (2005).

32. N. Shao, Gavriilidis.A. and P. Angeli, Chem.Eng.Sci **64**, 2749-2761 (2009).

33. Rebrov.E.V, Theoretical Foundations of Chemical Engineering **44**, 355-367 (2010).

34. J. Park, Z. Nie, A. Kumachev and E. Kumacheva, Soft Matter **6**, 630-634 (2010).

35. A. Gunther, M. Jhunjhunwala, M. Thalmann, M. Schmidt and K. Jensen, Langmuir **21**, 1547-1555 (2005).

36. Bird.R.B., Stewart.W.E. and Lightfoot.E.N., *Transport Phenomena*, 2nd Edition ed. (WILEY, NEW YORK, 2007).

37. Frank.M.J.W., Kuipers.J.A.M. and v. Swaaij.W.P.M., J.Chem.Eng.Data **41** (2), 297-302 (1996).

38. Tamimi.A, Rinker.E.B and Scandall.O.C, J.Chem.Eng.Data **39**, 330-332 (1994).

39. Himmelblau.D.M., Chem.Rev. **64** (5), 527-550 (1964).

40. Dalmolin.I, Skovroinski.E, Biasi.A, Corazza.M.L, Dariva.C and V. Oliveira.J, Fluid Phase Equilibria **245**, 193-200 (2006).

41. Won.Y.S., Chung.D.K. and Mills.A.F., J.Chem.Eng.Data **26** (2), 140-141 (1981).

42. Takahashi.M., Kobayashi.Y. and Takeuchi.H, J.Chem.Eng.Data **27** (3), 328-331 (1982).

43. Schnabel.T., Vrabec.J. and Hasse.H., Fluid Phase Equilibria **233** (2), 134-143 (2005).

44. Miyano.Y and Fujihara.I, Fluid Phase Equilibria **221**, 57-62 (2004).

45. Kolb.W.B. and Cerro.R.L., Chem.Eng.Sci **46** (9), 2181-2195 (1991).

46. Peng.X.F., Tien.Y. and Lee.D.J., Int.J.Heat.Mass Transfer **44** (15), 2957-2964 (2001).

47. Li.J. and Cheng.P., Int.J.Heat.Mass Transfer **47** (12-13), 2689-2698 (2004).